

Explainable AI for microseismic event detection

Ayrat Abdullin^a, Denis Anikiev^b, Umair bin Waheed^a

^a*Department of Geosciences, King Fahd University of Petroleum and Minerals, Dhahran, 31261, Saudi Arabia*

^b*Center for Integrative Petroleum Research, King Fahd University of Petroleum and Minerals, Dhahran, 31261, Saudi Arabia*

Abstract

Deep neural networks like PhaseNet show high accuracy in detecting microseismic events, but their black-box nature is a concern in critical applications. We apply explainable AI (XAI) techniques, such as Gradient-weighted Class Activation Mapping (Grad-CAM) and Shapley Additive Explanations (SHAP), to interpret the PhaseNet model's decisions and improve its reliability. Grad-CAM highlights that the network's attention aligns with P- and S-wave arrivals. SHAP values quantify feature contributions, confirming that vertical-component amplitudes drive P-phase picks while horizontal components dominate S-phase picks, consistent with geophysical principles. Leveraging these insights, we introduce a SHAP-gated inference scheme that combines the model's output with an explanation-based metric to reduce errors. On a test set of 9,000 waveforms, the SHAP-gated model achieved an F1-score of 0.98 (precision 0.99, recall 0.97), outperforming the baseline PhaseNet (F1-score 0.97) and demonstrating enhanced robustness to noise. These results show that XAI can not only interpret deep learning models but also directly enhance their performance, providing a template for building trust in automated seismic detectors.

Keywords: microseismic detection, explainable AI, Grad-CAM, SHAP, interpretability

1. Introduction

Microseismic monitoring detects and picks seismic events of very small magnitude, and it has greatly benefited from deep learning models in recent years. For instance, phase-picking neural networks such as PhaseNet (Zhu and Beroza, 2019) and the Earthquake Transformer (Mousavi et al., 2020) are capable of automatically detecting P- and S-wave arrivals in continuous data, significantly speeding up the process of event cataloging. Additionally, other architectures have demonstrated notable effectiveness in various applications, including seismic facies classification (Noh et al., 2023) and full-waveform inversion (Edigbue et al., 2025). These models frequently demonstrate superior performance compared to traditional methods in terms of accuracy and sensitivity. Nonetheless, a prominent challenge is that these models function as “black boxes”, which complicates the ability of seismologists to comprehend or have confidence in their decisions (Guo et al., 2023; Trani et al., 2022). In high-stakes geoscience contexts, such as monitoring induced seismicity for CO₂ storage or mining, the absence of interpretability presents significant challenges, as reliability and transparency are crucial.

Recent studies have brought to light particular challenges related to interpretability concerning phase-picking networks. For instance, the output score from PhaseNet represents a probability ranging from 0 to 1 at each time sample, which does not consistently align with the actual confidence of a pick. Park et al. (2024) noted that the prediction scores for both true and

false picks can be inconsistently high or low, making it hard to set a threshold that cleanly separates real events from noise. In other words, these models' output probabilities "do not necessarily correspond with the reliability" of the detection. Moreover, as noted by Myren et al. (2025), even when models such as PhaseNet appear highly accurate, their performance can fluctuate due to stochastic training and data-sampling variability, highlighting the need for evaluation frameworks that explicitly quantify model uncertainty alongside accuracy. Consequently, two challenges emerge: (1) domain experts find it difficult to assess the level of trust they can place in an automated pick, and (2) there is ambiguity regarding which characteristics of the waveform influenced the model's decision-making process. The lack of clarity surrounding this issue impedes the implementation of AI models in regular seismic monitoring, as professionals are hesitant to respond to detections that are not fully comprehensible to them.

Explainable AI (XAI) techniques present a valuable approach to tackle these challenges by shedding light on the inner workings of black-box models. In the field of geosciences, XAI has been increasingly recognized as a valuable approach for validating model behavior in relation to established domain knowledge. For example, feature-attribution methods such as SHAP and LIME have been applied in various contexts, including seismic facies classification (Saikia et al., 2019; Lubo-Robles et al., 2022; Bedle and Lubo-Robles, 2024), full-waveform inversion (Edigbue et al., 2025), and earthquake spatial probability assessment (Jena et al., 2023), to determine which input attributes influence the model's predictions. These methods, frequently referred to as post-hoc, serve to elucidate a model's workings after it has been

trained. They effectively "peel back" the black box, revealing whether the features deemed important by the model correspond with geophysical intuition or established factors.

In the area of seismic signal analysis, applications of XAI are just starting to surface, yet initial findings are promising. Trani et al. (2022) pioneered the application of activation visualizations for a 1D CNN detector, superimposing filter outputs on the raw waveform to identify which time segments activated the response of the network. Their qualitative "heatmaps" revealed that high-energy onset arrivals of P-waves significantly activated specific convolutional filters. Bi et al. (2021) introduced a refined Grad-CAM approach tailored for time-series data, known as EUG-CAM. This method projects the learned features of a CNN back onto the time-frequency domain. Through the process of upsampling the activations from the final convolutional layer, the researchers generated high-resolution explanation plots. These plots notably illustrated a surge of high-frequency energy coinciding with the arrival of the P-wave, which emerged as a critical characteristic for the classification of a microseismic event. Saliency-based methods have shown that deep networks tend to concentrate on seismic characteristics that are recognizable to humans, even in the absence of explicit instructions.

In addition to visual heatmaps, other researchers have utilized Layer-wise Relevance Propagation (LRP) and similar techniques to explore waveform classifiers. Majstorović et al. (2023) applied LRP to a single-station earthquake detector CNN and could thus trace which parts of the input contributed most to a detection. They found that the CNN had in fact learned to recognize where an earthquake's signal is within a long window (something

not given during training) and that many of the network’s salient features corresponded to physical aspects of the signal, such as the P-wave and S-wave portions and their frequency content. Notably, their analysis uncovered distinctions between the strategy employed by the CNN and that of a human analyst or a traditional STA/LTA trigger. This highlights that the model occasionally relies on more nuanced features that may not be apparent through visual inspection. In a similar vein, Jiang et al. (2024) utilized LRP on a microseismic classification model to analyze both accurate and inaccurate choices. In the context of true events, LRP verified that the network was focused on relevant waveform characteristics, such as a sudden increase in amplitude indicating an arrival, while for noise, it assisted in diagnosing failure modes. For instance, a false positive where the model was “fooled” by a transient noise spike, or a missed event where the signal lacked the frequency characteristics the model expected. These studies demonstrate how post-hoc explanations can expose the question of whether a model’s “reasoning” corresponds with geophysical reality and assist in identifying the reasons behind its misclassification of certain cases.

Even with these advancements, a significant gap in the existing literature is the application of SHAP (Shapley additive explanations) in deep seismic waveform models. SHAP represents a robust game-theoretic method that allocates an importance value to each feature for a specific prediction. Nonetheless, the direct application of SHAP to high-dimensional inputs, such as time series data, poses significant challenges. In microseismic monitoring, each waveform may contain thousands of sample points (features), which renders classical SHAP analysis both computationally demanding and challenging to

interpret in its raw form. Consequently, to our knowledge, no prior work has reported using SHAP on a CNN-based microseismic event detector. Although SHAP has proven useful in interpreting models for various geophysical tasks, including full-waveform inversion (Edigbue et al., 2025), seismic data denoising (Antariksa et al., 2025), and regional earthquake hazard assessment (Jena et al., 2023), its use in the specific area of high-temporal-resolution waveform phase detection has yet to be investigated. Our objective is to address this gap by illustrating the ways in which SHAP can be tailored for time-series seismic data. By aggregating SHAP values meaningfully (for example, summing contributions over time segments or sensor components), we extract clear insights from PhaseNet’s internal decision logic.

In this article, we make two important contributions. First, we apply Grad-CAM and SHAP to PhaseNet to interpret its microseismic event detection behavior. PhaseNet is a widely used phase-picking model (originally developed for earthquake P/S arrival timing) that we have adapted for microseismic binary (signal vs. noise) event detection. Using XAI, we reveal which parts of the waveform and which sensor components PhaseNet relies on for detecting events. Second, we go beyond interpretation by using the XAI results to enhance PhaseNet’s performance. We develop a simple yet effective SHAP-gated inference scheme that uses the explanation (SHAP values) to decide whether to accept or reject a detection. By incorporating this scheme, we improve the precision and recall of PhaseNet on a real microseismic dataset. To the best of our knowledge, this is the first instance in seismic event detection where explanations are used to inform the model’s output in a closed-loop fashion. This approach represents a developing trend in which

XAI is utilized not just for interpretation but also for enhancing performance directly. This is illustrated in various fields, including the use of XAI for data augmentation in seismic denoising (Antariksa et al., 2025), predicting ground-motion parameters (Sun et al., 2023), and in adjacent fields, e.g., for enhancing damage recognition accuracy in building damage detection (Wang et al., 2025). Our findings demonstrate that the approach we employed results in a detector that is both more consistent and trustworthy, effectively tackling the reliability concerns highlighted by previous researchers. Our study primarily examines PhaseNet; however, in the Discussion section, we explore the potential application of these explainability techniques to other emerging models, such as Transformer-based detectors, and consider how XAI can play a crucial role in the deployment of geophysical AI models.

2. Materials and Methods

2.1. Microseismic Dataset and PhaseNet Model

Our evaluation of the explainable AI approach involves utilizing a dataset comprised of microseismic waveforms, which capture the characteristics of minor induced earthquakes, along with noise recordings. The dataset comprises labeled waveform windows, with a consistent length of 30 seconds each, obtained from continuous recordings in a practical monitoring setting. Each window is assigned a binary label: signal (event) if it contains a microseismic arrival, or noise if no event is present. We curated a balanced dataset of approximately 10,000 windows, split into a training set (100 windows) and a test set (9,000 windows). The signals in this dataset are low-magnitude seismic events (in the order of $0.5 < M < 2.5$) from a surface geophone array,

with clear P-wave and S-wave onsets, superimposed on ambient noise. Examples of noise encompass instrument noise as well as a range of non-seismic transients that are characteristic of the field environment. All waveforms are preprocessed with amplitude normalization, which is standard for microseismic detection. We use three-component recordings (East-West, North-South, vertical) so that phase polarity differences can be leveraged by the model.

Our base detection model is PhaseNet (Zhu and Beroza, 2019), a deep convolutional neural network originally designed for picking P and S phase arrival times. PhaseNet’s architecture follows a U-Net style fully convolutional network with an encoder-decoder structure (Figure 1). In our implementation, the model takes a multi-component waveform window as input and produces as output a set of probability traces – one for each class of interest (noise, P arrival, S arrival). For binary event detection, we interpret the PhaseNet output as a single probability of “event present” within the window, derived from the maximum predicted likelihood of a P or S arrival in that window. Essentially, if PhaseNet produces a class probability that exceeds a chosen threshold for either the P or S channel within the window, the window is classified as containing an event. We tested the PhaseNet on our microseismic dataset using supervised learning: windows with actual events were labeled positive, and noise-only windows were negative. The pre-trained PhaseNet achieved 97% classification accuracy on the held-out test set, corresponding to high initial precision and recall (details in Section 3). However, like prior studies, we observed that setting an optimal decision threshold on the PhaseNet output was non-trivial. A simple 0.5 probability cutoff was not satisfying, and tuning the threshold involved trading off false

negatives versus false positives. This observation motivated us to investigate the incorporation of explainability metrics into the decision process.

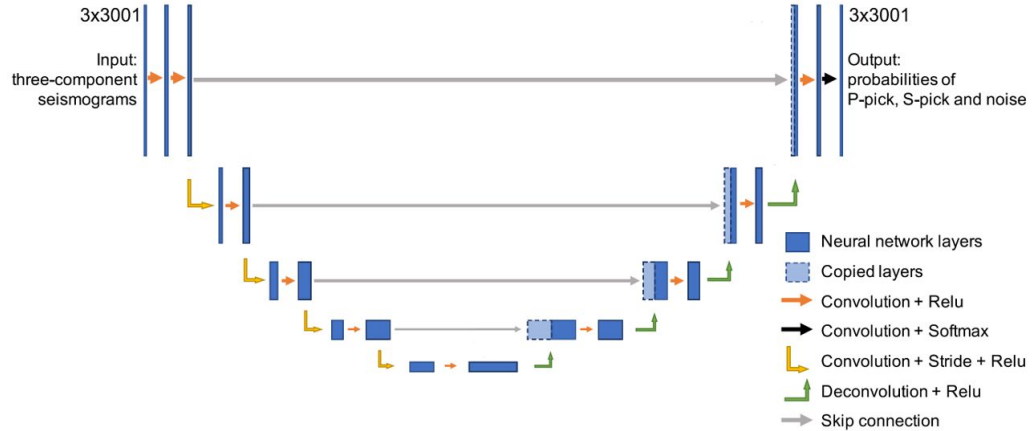


Figure 1: Schematic illustration of the network architecture. The input consists of 30-s three-component seismograms sampled at 100 Hz, yielding an input dimension of 3×3001 . The network outputs three probability sequences of equal length, corresponding to P-pick, S-pick, and noise classes. Blue rectangles indicate neural network layers. Arrows denote operations, as summarized in the lower right corner. The model comprises four stages dedicated to down-sampling and four stages for up-sampling. Down-sampling is carried out using 1-D convolutions with a kernel size of 7 and a stride of 4. In contrast, up-sampling is performed through deconvolutions, which serve to restore the sequence length from the previous stage. Skip connections combine feature maps from each down-sampling stage with the corresponding up-sampling stage (indicated by dashed rectangles), thereby aiding in convergence. The last layer utilizes a softmax activation function to produce class probabilities (adapted from Zhu and Beroza (2019)).

2.2. Grad-CAM for Waveform Data

To interpret which parts of a waveform influence PhaseNet’s predictions, we applied the Gradient-weighted Class Activation Mapping (Grad-CAM)

technique (Selvaraju et al., 2017). Grad-CAM is a general method that produces a coarse “heatmap” of importance by using the gradients of the target class score with respect to the convolutional layers of the network. In image applications, Grad-CAM highlights image regions most responsible for a classification; here, we adapt it to 1D time-series data. We followed the procedure of Selvaraju et al. (2017) in the context of our 1D CNN: we fed a waveform through PhaseNet and obtained the event probability output. We then computed the gradient of that output (for a given window) with respect to the feature maps of the final convolutional layer. When these gradients are averaged globally across all time positions, they provide weights that reflect the significance of each filter’s activation in relation to the event prediction. Next, we took a weighted linear combination of the feature maps (of the final convolutional layer) using these gradient-derived weights, and then applied a ReLU (rectified linear unit) to keep only positive influences. The result is a coarse activation map across the time dimension, which we then linearly interpolated to the original waveform length to obtain a time series of “importance scores” – the Grad-CAM heatmap. It is essential to recognize that by utilizing the final convolutional layer, Grad-CAM emphasizes high-level semantic features, albeit at the expense of spatial resolution. Researchers have observed that this may obscure fine-grained details and have suggested alternative strategies, including optimal layer selection (Yoo and Jeong, 2022) and the fusion of heatmaps from multiple layers (Li et al., 2023), to tackle this trade-off. In the context of this research, the conventional Grad-CAM method was considered adequate for identifying the main P- and S-wave energy packets.

In practice, we generated Grad-CAM explanations for many test examples, both true events and noise. The Grad-CAM output for each waveform was then overlain on the waveform plot for visualization. This allowed us to see, for example, if the network was focusing on the P-wave onset, the S-wave arrival, or perhaps some noise burst. It should be noted that standard Grad-CAM can miss features that have a negative influence on the prediction (since the ReLU truncates negative gradients). However, since we are primarily interested in what supports an event detection (the positive evidence), this was acceptable. For completeness, one could use guided backpropagation or LRP to capture inhibitory factors, but that was beyond our scope. Our Grad-CAM implementation yields an approximate explanation of where PhaseNet “looks” in time to decide if a window contains an event.

2.3. SHAP Value Analysis

While Grad-CAM provides a visual localization of important regions, it does not quantify the contribution of each input feature. We therefore turned to Shapley additive explanations (SHAP; Lundberg and Lee (2017)) to attribute an importance value to every sample in the waveform. SHAP interprets the prediction of a model by computing the contribution of each feature (input dimension) toward the difference between the model’s output and a baseline output. Intuitively, a positive SHAP value for a given sample (at a specific time and component) means that the sample increased the model’s confidence in the event class, whereas a negative value means it pushed the model toward predicting noise.

Directly computing Shapley values for every sample in a long seismic waveform is intractable, so we simplified the problem by focusing on component-

level attributions. For each waveform window, we generated all possible combinations of masked components (E, N, Z) with either the true signal or a baseline replacement (zero or mean). This yields the full set of $2^3 = 8$ coalition values, from which exact Shapley contributions can be computed without approximation. For each subset, we evaluated PhaseNet’s detection score (e.g., maximum P or S probability in the window) and then applied the Shapley value formulas to estimate the marginal contribution of each component. The resulting importance rankings ϕ_E , ϕ_N , ϕ_Z for P and S channels quantify how much each component contributes to the detection. This component-masking approach thus provides interpretable, mathematically grounded attributions while remaining computationally efficient.

Let $\mathbf{X} \in \mathbb{R}^{3 \times L}$ be a single three-component window (E, N, Z) with $L = 3001$ samples. For a coalition mask $\mathbf{m} = (m_E, m_N, m_Z) \in \{0, 1\}^3$, we form

$$\mathbf{X}^{(\mathbf{m})} = \mathbf{m} \odot \mathbf{X},$$

where \odot denotes broadcasting and element-wise multiplication. The dropped channels are replaced by zeros (baseline). Let $f(\cdot)$ be PhaseNet’s softmax output and $c \in \{N, P, S\}$ the target class index. The score of a (possibly masked) window is

$$V_{\mathbf{m}} = v(\mathbf{X}^{(\mathbf{m})}; c) = \max_{1 \leq t \leq L} f_c(\mathbf{X}^{(\mathbf{m})})_t.$$

With three channels, we evaluate the eight coalitions

$$V_{000}, V_{100}, V_{010}, V_{001}, V_{110}, V_{101}, V_{011}, V_{111},$$

where, e.g., V_{100} keeps only E, V_{011} keeps N and Z, etc. With $n = 3$ features, the Shapley weight for a subset S not containing i is $w(|S|) = \frac{|S|!(n-|S|-1)!}{n!}$,

i.e., $w(0) = \frac{1}{3}$, $w(1) = \frac{1}{6}$, $w(2) = \frac{1}{3}$. The channel attributions ϕ_E, ϕ_N, ϕ_Z for a single window are

$$\boxed{\begin{aligned}\phi_E &= \frac{1}{3}(V_{100} - V_{000}) + \frac{1}{6}(V_{110} - V_{010}) + \frac{1}{6}(V_{101} - V_{001}) + \frac{1}{3}(V_{111} - V_{011}), \\ \phi_N &= \frac{1}{3}(V_{010} - V_{000}) + \frac{1}{6}(V_{110} - V_{100}) + \frac{1}{6}(V_{011} - V_{001}) + \frac{1}{3}(V_{111} - V_{101}), \\ \phi_Z &= \frac{1}{3}(V_{001} - V_{000}) + \frac{1}{6}(V_{101} - V_{100}) + \frac{1}{6}(V_{011} - V_{010}) + \frac{1}{3}(V_{111} - V_{110}).\end{aligned}}$$

In a general case, for a batch of N windows, we report per-channel importance as the mean absolute Shapley value:

$$\text{Imp}_j = \frac{1}{N} \sum_{n=1}^N |\phi_j^{(n)}|, \quad j \in \{E, N, Z\}.$$

The SHAP component importance refers to the total contribution attributed to an entire component of the sensor. We summarized the SHAP results by computing, for each class (event vs. noise), the average contribution of each component (E, N, Z). In addition, we recorded how often a given component provided the largest SHAP value, that is, how frequently that channel contributed the most to the model's decision compared with the other two. These metrics help relate the model's behavior to the known seismic wave propagation characteristics. We also created SHAP summary plots where each dot represents a feature (time sample) colored by component, plotted against its SHAP value – this visualizes the spread and magnitude of contributions for signals and noises.

It is worth noting that SHAP values offer a signed attribution – some inputs can actually lower the event probability. In our case, however, we found that most features with significant magnitude had positive SHAP values for true events (they added to the likelihood of an event). Negative contributions

were typically small and associated with scattered noise oscillations, which slightly push the model towards the “no-event” decision. For simplicity and interpretability, we focused on the positive SHAP contributions as indicators of features that support the presence of an event.

2.4. SHAP-Gated Inference Scheme

Beyond offline analysis, we integrated the explainability results into the PhaseNet’s decision logic. Our approach, termed SHAP-gated inference, uses a combination of SHAP values to classify a waveform as an event. The rationale comes from our observation that true events tend to produce not only a high model probability but also multiple significant SHAP contributions, whereas false positives often have only one weak transient indication of evidence (either in probability or SHAP). We therefore defined two metrics for each window: (1) the PhaseNet output probability of an event (specifically, the maximum P-or-S probability in the window), and (2) the SHAP “mean6”, defined as the mean of the 6 SHAP values (E, N, Z for both P- and S-wave probabilities) in that window. Through exploratory analysis on the training set, we found that taking the mean of SHAP feature contributions gave a robust summary of the “amount of explanatory evidence” in a detection. Intuitively, a real event might trigger several strong features (e.g., P onset on Z component, S onset on horizontals, etc.), yielding 6 high SHAP values whose mean is large. A spurious detection might only have one or two moderate features, and then the mean of six (including some zeros or low values) would be much lower.

Our decision rule is as follows: for each window, we compute six absolute

Shapley values:

$$\{ |\phi_{P,E}|, |\phi_{P,N}|, |\phi_{P,Z}|, |\phi_{S,E}|, |\phi_{S,N}|, |\phi_{S,Z}| \}.$$

The decision statistic is their mean,

$$S_6 = \frac{1}{6} \left(|\phi_{P,E}| + |\phi_{P,N}| + |\phi_{P,Z}| + |\phi_{S,E}| + |\phi_{S,N}| + |\phi_{S,Z}| \right).$$

With a threshold $SHAP$, the classification rule is

$$\hat{y} = \mathbf{1}[S_6 \geq SHAP],$$

i.e., the window is labeled as a signal if and only if the average SHAP importance across all six (P/S \times components) exceeds the threshold.

We optimized the thresholds ($PROB$, $SHAP$) on the training set by sweeping values to maximize the F1-score (the harmonic mean of precision and recall). We then fixed these thresholds and applied the rule to the test set to evaluate the improvement in detection performance (see Section 3.3). It's essential to note that the thresholds are dimensionless, but they are tied to our data normalization and model output scaling. In another setting, they would need recalibration. In effect, this SHAP-gating constitutes a simple post-hoc decision fusion, combining the model's numeric output with an XAI-based feature metric.

3. Results

3.1. Grad-CAM Reveals Model Focus on Seismic Phases

Grad-CAM visualizations provided clear insights into which waveform segments PhaseNet relied on for event detection. Figure 2 shows examples

for three representative cases: a high-SNR event, a low-SNR event, and a pure noise window.

For the high-SNR event (Fig. 2a, 3a), Grad-CAM activations are sharply concentrated around the manually picked P arrival. A secondary but weaker highlight is visible at the S arrival. The zoomed view (Fig. 3a) illustrates that the importance scores extend across several tens of samples around the onset, indicating that PhaseNet bases its decision not just on the very first sample but on the characteristic onset pattern.

Importantly, outside of these arrival times, the Grad-CAM values are much smaller. Thus, the background coda and noise in the rest of the window do not strongly influence the model. This focus on real seismic phases gives us confidence that PhaseNet’s internal logic is geologically/plausibly sound, rather than latching onto unrelated artifacts. Similar observations have been reported by other authors using different explanation methods; for example, Majstorović et al. (2023) found that their CNN detector clearly “learned to recognize where the earthquake is within the sample window” via relevance mapping.

In the low-SNR event (Fig. 2b, 3b), the attributions continue to correspond with the approximate P- and S-wave neighborhoods, but the responses are less sharply picked and more spread out than in the high-SNR case. This shows that the model still pays attention to the right parts of the waveform, even when there is more noise, but with less confidence and a wider time range.

In comparison, the noise-only example (Fig. 2c) shows a lack of coherent Grad-CAM focus. The activation is weak and scattered across the entire

window without clustering near any particular onset. This pattern is consistent with a correct noise classification: the model doesn't find any phase-like features that would support an event label.

These results show that PhaseNet's convolutional filters mostly focus on parts of the P and S arrivals that have physical meaning, even when the SNR changes. The lack of structured activations in noise windows reinforces the idea that the model is not just reacting to random spikes, but is also sensitive to real seismic phase patterns. These qualitative insights enhance confidence in PhaseNet's internal decision-making process and validate the subsequent quantitative attribution analysis.

3.2. SHAP Highlights Key Features and Component Contributions

The SHAP analysis demonstrated distinct variations in the reliance of PhaseNet on each component for classifying P- and S-phases. Table 1 shows the average absolute Shapley values with confidence intervals and the percentage of cases in which each component is the most important. For P-class detections on signal windows, the vertical (Z) component has the biggest effect, with a mean contribution of 0.30 and being the most important in 50% of cases. This proves that PhaseNet primarily uses vertical ground motion to find P-wave arrivals. For S-class detections, on the other hand, the horizontal components (E and N) are more important, with mean SHAP values of 0.36 and 0.33, and they are the most common in 46–51% of cases. This is what seismologists expect, since S-wave energy is mostly recorded on horizontals.

To further illustrate these component-level trends, Figure 4 shows the distributions of absolute SHAP values for predictions in the P- and S-class. For signal cases (4a,c), SHAP values for the P-class cluster tightly around

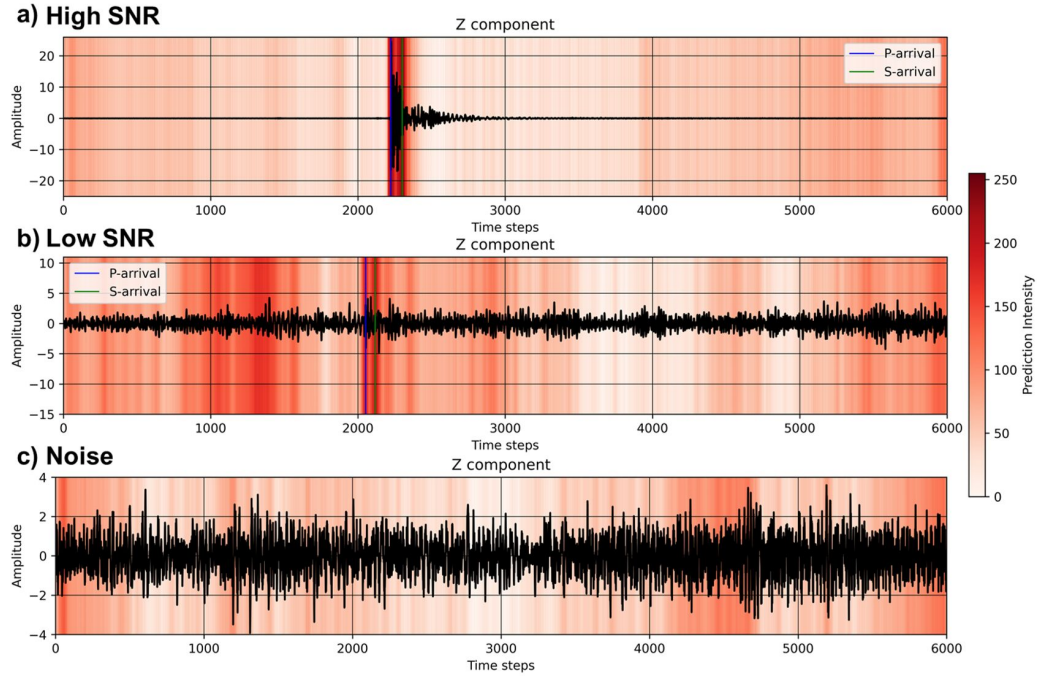


Figure 2: Grad-CAM visualizations of PhaseNet attention on the vertical (Z) component for three representative cases: (a) a high-SNR event with clear P- and S-wave arrivals, (b) a low-SNR event, and (c) a noise-only window. The heatmaps show Grad-CAM attribution intensity (red shading) overlaid on the waveform amplitude. Darker shades correspond to stronger model attention. For high-SNR events, attention is sharply concentrated around the P-wave onset with secondary activation near the S arrival; for low-SNR events, the attention remains aligned with the arrivals but becomes broader and less intense; for noise, attention is diffuse and unstructured, indicating no consistent phase-like focus.

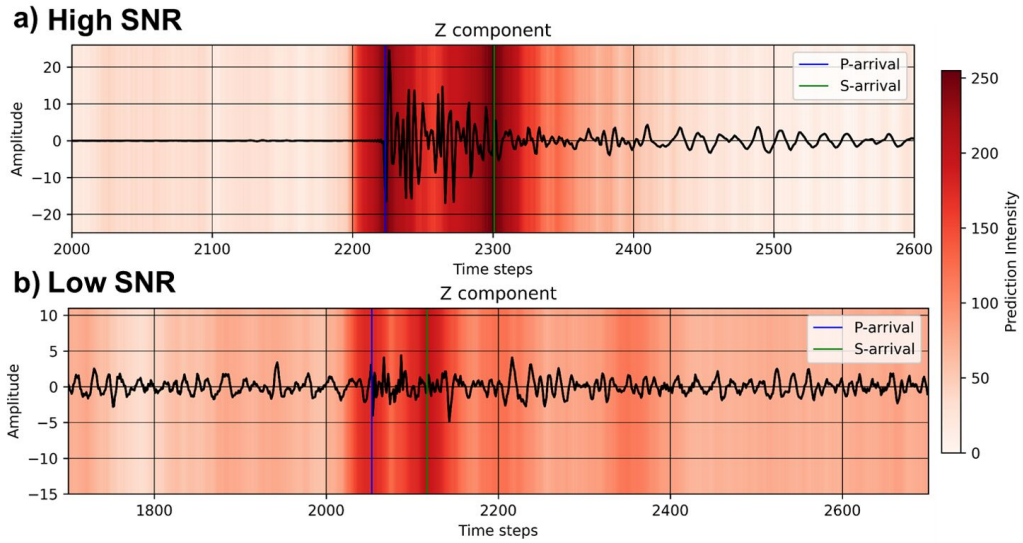


Figure 3: Zoomed-in Grad-CAM views of the vertical (Z) component for (a) a high-SNR and (b) a low-SNR event, corresponding to Figure 2a–b. The heatmaps emphasize the specific areas where the model exhibits the greatest emphasis in distinguishing between P- and S-waves arrivals. The high-SNR example illustrates a distinct and clearly defined activation centered on the arrival of the P component, while, in the low-SNR scenario, there is a broader and less pronounced area of focus, which suggests a decrease in model confidence when faced with noisy conditions.

0.25 on the Z component, whereas the S-class shows higher contributions on the horizontal E and N channels, consistent with shear-wave polarization. For noise windows (Fig. 4b,d), on the other hand, all components show very low SHAP magnitudes (< 0.1) with no clear separation. This means that there is no coherent seismic-phase evidence. These histograms support the statistical patterns shown in Table 1, confirming that PhaseNet’s attributions show real differences between the physics of P and S waves.

Figure 5 presents violin plots that effectively illustrate these trends. In the case of signal windows, the SHAP distributions exhibit a pronounced elevation centered around the arrivals of P- and S-waves (see Fig. 5a,c), while for noise windows (Fig. 5b,d) the values are much smaller and broadly distributed. In noise, mean SHAP values are only 0.06 (P-class) and 0.02 (S-class), confirming the lack of coherent explanatory evidence in the absence of true seismic phases. Notably, even though Z occasionally shows slightly higher noise attributions, these remain an order of magnitude weaker than for true events.

These findings collectively illustrate that PhaseNet’s attributions correspond with physical reality: Z predominates P-phase detections, while E and N prevail S-phase detections, and noise windows do not have any significant explanatory signal. This shows that PhaseNet not only attains a high level of accuracy, but it also uses features that have real-world meaning, which builds trust in its decision-making process. These observations led us to consider that by employing the model output to calculate the SHAP values, we can address certain misclassification errors. If we see a SHAP signature of an event, perhaps the detection should be accepted even if the raw probability

was marginal. Likewise, if the model output is high but the SHAP evidence is not convincing, perhaps the detection should be discarded. This forms the basis of the SHAP-gated inference, the results of which we present next.

Table 1: Mean absolute SHAP values ($|\phi|$), 95% confidence intervals (CI), and dominance percentages for each component (E, N, Z) across signal and noise windows. Values are reported separately for P-class and S-class predictions.

Component	P-class				S-class			
	Mean $ \phi $	CI _{lo}	CI _{hi}	% Dominant	Mean $ \phi $	CI _{lo}	CI _{hi}	% Dominant
E (signal)	0.31	0.31	0.31	15.1	0.36	0.36	0.37	50.5
N (signal)	0.33	0.32	0.33	35.2	0.33	0.33	0.34	45.6
Z (signal)	0.30	0.30	0.30	49.7	0.19	0.19	0.20	3.9
E (noise)	0.06	0.06	0.06	24.3	0.02	0.02	0.02	24.2
N (noise)	0.07	0.06	0.07	24.4	0.02	0.02	0.02	23.0
Z (noise)	0.10	0.10	0.10	51.4	0.02	0.02	0.02	52.8

3.3. Improved Detection Performance with SHAP-Gated Inference

The central practical outcome of this study is that incorporating SHAP-based criteria into PhaseNet’s decision process improves its reliability, not only under clean conditions but also as noise levels increase. The optimal values for the training set of 100 samples (50 signals and 50 noise) were found to be $PROB = 0.87$ and $SHAP_{mean6} = 0.18$. This means PhaseNet alone had to be >0.87 confident to trigger an event on probability alone; otherwise, we required a substantial SHAP evidence mean of 0.18 (in normalized units) to accept the event. We then evaluated the performance of the baseline model versus the SHAP-gated model on a balanced test set of 9,000 windows (4,500 true events and 4,500 noise).

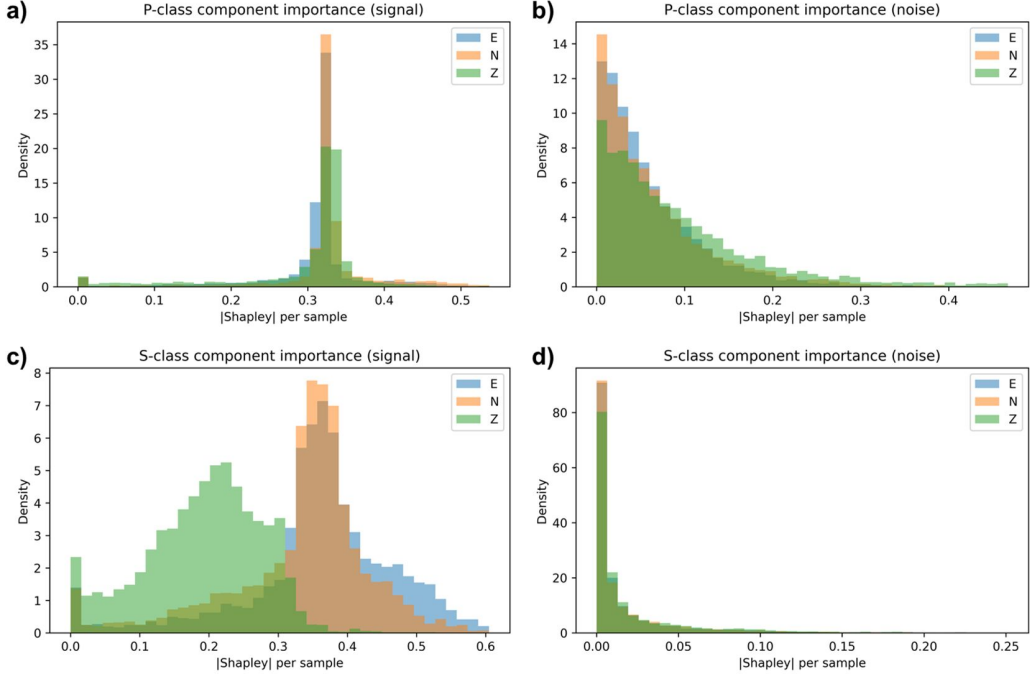


Figure 4: Distributions of absolute SHAP values ($|\phi|$) for 5,000 signal and 5,000 noise windows. Panels (a,b) show P-class attributions, and panels (c,d) show S-class attributions, separated by component (E, N, Z). For signal windows, vertical (Z) contributions slightly dominate the P-class, while horizontal components (E and N) dominate the S-class. Noise windows show SHAP magnitudes that are low across all components, which means that there is no clear evidence for either phase class. These distributions complement the summary statistics in Table 1.

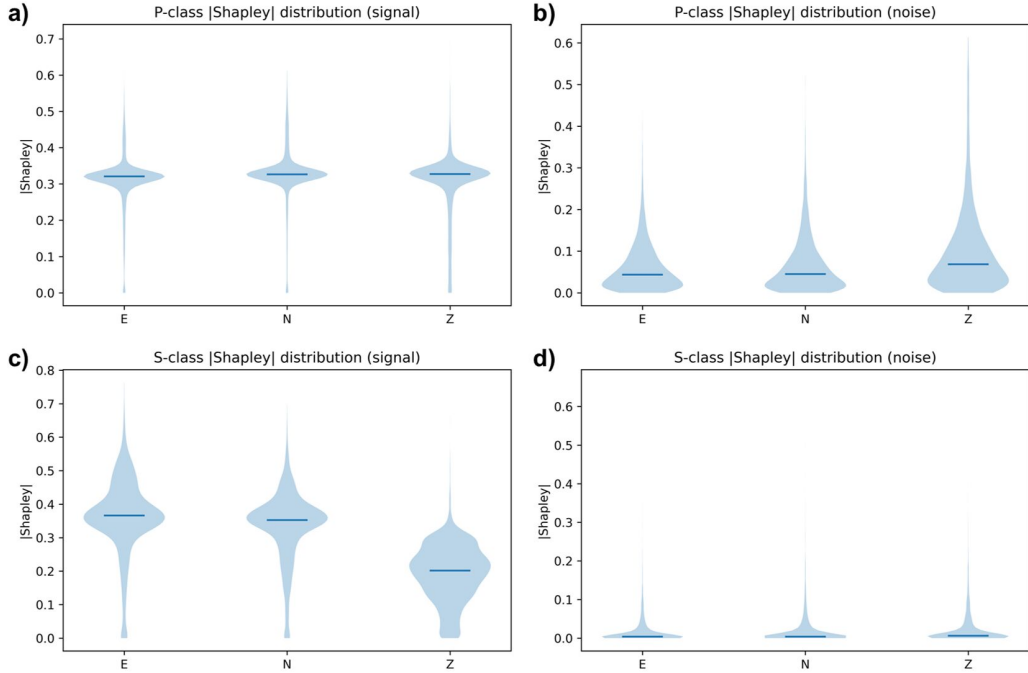


Figure 5: Violin plots of Shapley value distributions for 5,000 signal and 5,000 noise windows. (a) P-class SHAP distributions for signal windows; (b) P-class for noise; (c) S-class for signal; (d) S-class for noise. Signal windows show strong and coherent SHAP concentrations: the vertical (Z) component dominates P-phase detections, while horizontals (E and N) dominate S-phase detections. Noise windows exhibit uniformly low SHAP values across all components. Summary statistics are provided in Table 1.

On the clean dataset, the baseline PhaseNet (probability-only thresholding at 0.87) achieved an F1 score of 0.97, with a precision of 0.99 and a recall of 0.96. This corresponds to 186 false negatives and 45 false positives. With the SHAP-gated rule ($SHAP_{mean6} = 0.18$), performance improved to an F1 of 0.98, with Precision = 0.99 and Recall = 0.97, reducing false negatives to 140. These improvements were achieved without retraining the network – simply by augmenting the decision rule with SHAP evidence.

Beyond clean conditions, we systematically tested robustness against increasing noise relative amplitude using both harmonic and random noise injection. For each relative amplitude, we ran five random cross-validation splits with a 100-sample balanced training set (50 signal, 50 noise) used to tune thresholds, and a separate 9,000-sample balanced test set for evaluation. This strict separation ensured that threshold optimization was not biased by the evaluation set.

The results are summarized in Figure 6. When there is harmonic noise, the probability-only baseline shows a steady drop in F1 as the noise amplitude goes up. By relative amplitude 1.7, performance is below 0.8. The *SHAP* criterion ("mean6 ONLY") consistently outperforms probability-only, keeping F1 above 0.8 even when noise levels are high. For random noise (green vs. red curves), the SHAP-based method again proves more resilient, sustaining near-constant $F1 > 0.95$ up to amplitude 1.6, whereas the probability-only rule degrades earlier.

When extending to even higher noise amplitudes (up to $5\times$, Fig. 7), both methods inevitably lose accuracy, but SHAP-based thresholding retains a clear advantage. At relative amplitudes around 2.0, the probability-only

baseline collapses to $F1 \approx 0.66$, while the SHAP-based approach still holds around $F1 \approx 0.75$. This margin is useful in practice because it means that the error rate goes down by 10 to 15% even when in highly challenging conditions.

Collectively, these experiments illustrate that SHAP-gated inference proves advantageous not only on "clean" test sets but also significantly improves resilience against increased noise levels. By necessitating adequate *SHAP* evidence, the system effectively eliminates spurious detections that would otherwise be accepted based solely on probability, while also ensuring that real events, which might be overlooked under conditions of degraded SNR, are accurately identified.

4. Discussion

Our findings demonstrate that explainable AI tools can play a dual role in seismic event detection: interpreting model behavior and enhancing model performance. We showed this in the context of PhaseNet, but the approach is general and opens several avenues for further exploration.

To our knowledge, this is the first study to integrate SHAP values into the inference process of a seismic detection model. Previous works have primarily used XAI for post-hoc interpretation – for example, visualizing that a CNN focuses on P-wave arrivals (Bi et al., 2021; Trani et al., 2022) or using LRP to debug misclassifications (Majstorović et al., 2023; Jiang et al., 2024). We extend those ideas by feeding the explanation back into decision-making. This places our work within the emerging field of 'explainable-by-design' performance enhancements, where the XAI component is an active part of the system pipeline, not merely a post-hoc analysis tool.

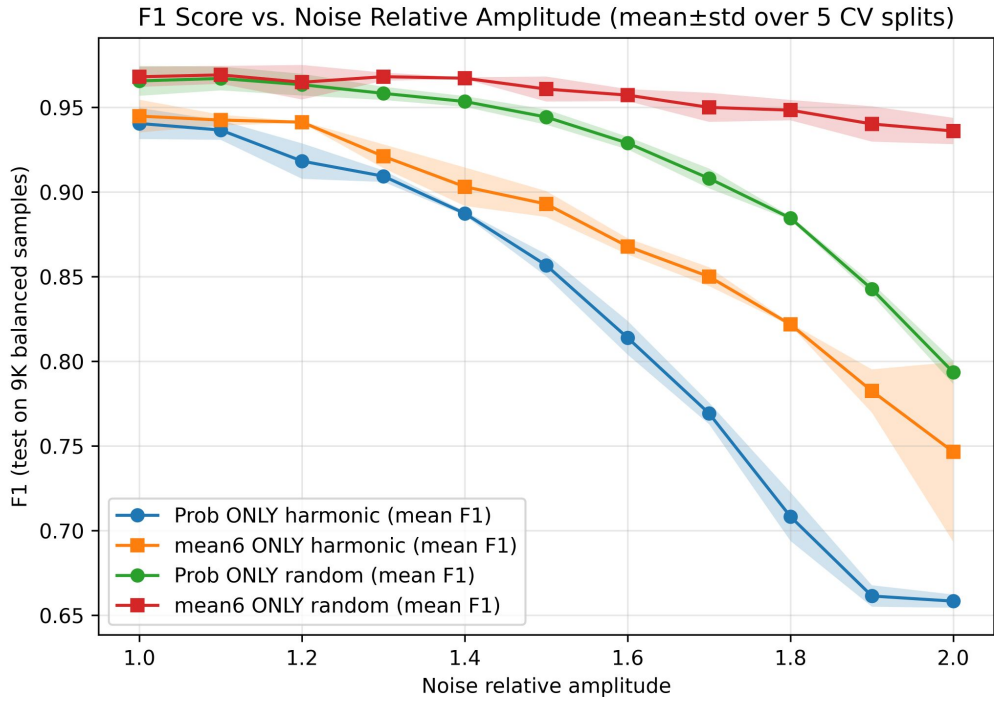


Figure 6: F1 score in relation to the relative amplitude of noise for both harmonic and random noise injections (mean \pm standard deviation across five cross-validation splits). The thresholds were adjusted individually for criteria based only on probability and *SHAP* using a 100-sample balanced train-set and then subsequently evaluated using a 9,000-sample balanced test set. The shaded areas around each curve show how the five CV splits differ from each other. Probability-only performance (blue, green) degrades steadily with increasing noise, while *SHAP*-based thresholding (orange, red; mean of 6 *SHAP* values) maintains substantially higher F1 across the entire range, demonstrating greater resilience to structured noise.

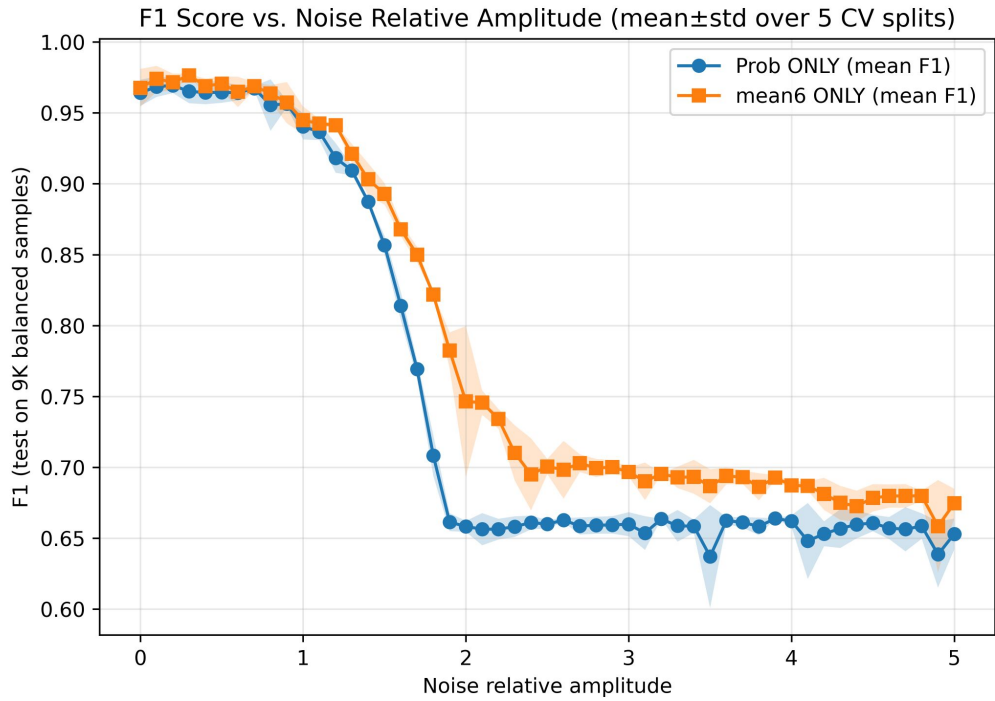


Figure 7: F1 score versus extended noise relative amplitude (up to 5.0) for probability-only (blue) and SHAP-only (orange) thresholding, averaged over five cross-validation splits. The shaded regions around each curve indicate variability across the five CV splits. Both methods perform worse as noise levels rise, but SHAP-based inference always does better than the baseline, keeping F1 at about 0.75 at amplitude 2.0 compared to about 0.65 for probability-only. This advantage shows the practicality of using SHAP evidence as the decision rule, even when there is considerable noise.

It is possible to draw a parallel with the research conducted by Antariksa et al. (2025), who employed a SHAP-based methodology to facilitate data contamination in the training of a seismic denoising network, similarly utilizing explanations to enhance model performance prescriptively. This approach is gaining traction in related geosciences applications. For instance, Wang et al. (2025) applied SHAP to a 1D-CNN model for structural damage identification. Their interpretability analysis allowed them to perform optimal feature selection, creating a refined model with fewer input features that achieved significantly higher accuracy than the original. While also using SHAP, Sun et al. (2023) focused on diagnostic validation rather than prescriptive enhancement. They confirmed that their machine learning model for predicting Peak Ground Acceleration (PGA) learned relationships consistent with established physical laws, thereby using explainability to build trust and verify the model’s scientific rationality. Our work aligns more closely with the former, using the explanation as a mechanism for direct performance improvement.

Our SHAP-gating strategy is similar to how a human analyst would check a detection: there should be a trigger (a spike in probability), and the waveform’s context and features should also make sense, for example, the right amount of energy on relevant components and the appropriate length. SHAP is, in a sense, quantifying that context for the model. Our approach’s success highlights the argument presented by Park et al. (2024) that a model’s raw output score does not consistently serve as a dependable measure of detection confidence. Their approach involved retraining the model using specific techniques aimed at enhancing the consistency of its scores in relation to signal

quality. In contrast, our approach maintains the integrity of the model while incorporating an external consistency check through *SHAP*. A promising avenue for future research involves integrating these methodologies: it would be beneficial to train a PhaseNet-like model incorporating a regularization term or a multi-task objective that specifically aims to enhance the *SHAP* mean for true events while reducing it for noise. This might directly reinforce the concept of “explanatory evidence” in the model’s learning process.

While we focused on PhaseNet (a specific CNN architecture for picking), the methodology applies to other seismic event detection models. For example, the Earthquake Transformer model, which employs self-attention and was specifically developed for regional earthquake detection, naturally generates attention weights that are subject to interpretation (Mousavi et al., 2020). It is possible to envision utilizing those attention scores in a manner akin to our *SHAP* metric for the purpose of filtering outputs. For instance, it is necessary to ensure that detection focuses its attention on an arrival. Likewise, simpler CNN or LSTM-based detectors in volcano seismology (Beker et al., 2022) or acoustic emission monitoring could benefit from Grad-CAM or SHAP analyses to ensure they respond to physically meaningful features. Additionally, these post-hoc methods may serve as a significant benchmark for validating and comprehending the behavior of intrinsically explainable models, such as the prototype-based neural networks suggested for seismic facies classification (Noh et al., 2023), thereby facilitating a comparison of various families of XAI approaches. For instance, in geophysics, Fourier Neural Operator (FNO) models (Li et al., 2020) can be used to find anomalies in continuous seismic wavefields. FNOs are highly complex, but applying XAI

to them (e.g., integrated gradients or SHAP on input frequency components) could reveal whether they’re picking up real seismic signals or artifacts. We anticipate that as more geophysical AI models come online, incorporating explainability will become a best practice to validate models before deployment.

We acknowledge several limitations of our study. First, our SHAP-gating rule was manually tuned and quite simple. It worked well for our balanced dataset, but in a real setting, the best thresholds might change if the noise levels change or if the characteristics of the events change (for example, bigger events might have different SHAP distributions than smaller ones). Recalibration or adaptive thresholding may be necessary in a production environment. Future research may investigate more advanced explanation-based metrics. For example, instead of just using the mean, one could come up with a metric based on the multi-layer fusion methods suggested for Grad-CAM (Li et al., 2023), which combine information from different levels of the network to make a stronger explanation. This could lead to a gating criterion that is responsive to both detailed onset characteristics (from shallower layers) and overall waveform morphology (from deeper layers). Second, our evaluation was performed on a controlled, balanced dataset (equal numbers of signal and noise windows). In a continuous monitoring stream, the strong class imbalance (many more noise than signal windows) means that even a small increase in false positives could accumulate into frequent false triggers. In our baseline case, the SHAP-gated rule slightly increased false positives (from 45 to 50) but significantly reduced false negatives (from 186 to 140), indicating a more sensitive detector that misses fewer true events.

This improvement in recall is particularly valuable for microseismic monitoring, where the cost of missed detections often outweighs occasional extra false alarms. The modest rise in false positives remains acceptable given that *SHAP* evidence integrates physically meaningful features (multi-component phase energy), which should remain robust under more complex noise conditions.

5. Conclusions

This study shows that explainable AI can be used for both model interpretation and improving detection in microseismic monitoring. We applied Grad-CAM to the PhaseNet model and visually verified that the network’s decision-making process is geophysically valid, concentrating on the P- and S-wave arrivals, confirming that a seismic event happened. Along with this, SHAP analysis gave quantitative, component-level attributions that are consistent with established physics of seismic wave propagation, which makes the model’s internal logic even more reliable.

More importantly, we have shown that these explanations can be actively added to the inference pipeline to make the detector more robust. Our new SHAP-gated inference scheme, which combines the model’s output probability with a measure of explanatory evidence, improved the F1-score by lowering the number of false negatives. This illustrates a significant new pathway for XAI in the geosciences, shifting from mere interpretation to proactive performance improvement. The enhanced resilience to noise demonstrated by the SHAP-gated model indicates that this method holds significant promise for practical monitoring situations where signal quality may fluctuate con-

siderably. The principles of explanation-guided inference, while illustrated using PhaseNet, are widely applicable to various deep learning models in seismology and other fields. Ultimately, by making AI models more transparent and leveraging their explanations to make them more reliable, we can accelerate the confident deployment of AI in critical geoscience applications.

Declaration of competing interest

The authors declare that they have no known competing financial interests or personal relationships that could have appeared to influence the work reported in this paper.

Data availability

The microseismic dataset underlying this article was provided by Seismik s.r.o. to be used in this study. This dataset will be shared on request to the corresponding author with permission of Seismik s.r.o.

Acknowledgments

We thank Dr. Leo Eisner from Seismik s.r.o. for graciously providing the data. We also thank KFUPM for its support and the Smart Earth Exploration and Monitoring group (SEEM) for constructive discussions.

Declaration of generative AI and AI-assisted technologies in the manuscript preparation process

During the preparation of this work, the authors used ChatGPT (OpenAI, USA) to refine the language and improve the readability of the manuscript.

After using this tool, the authors thoroughly reviewed and edited the content as needed and take full responsibility for the content of the published article.

References

Antariksa, G., Koeshidayatullah, A., Das, S., Lee, J., 2025. Xai-driven contamination for self-supervised denoising with pixel-level anomaly detection in seismic data. *Journal of Applied Geophysics* 238, 105723.

Bedle, H., Lubo-Robles, D., 2024. Application of vector plots, lime, and shap for seismic facies machine learning evaluation, in: SEG International Exposition and Annual Meeting, SEG. pp. SEG-2024.

Beker, T., Ansari, H., Montazeri, S., Song, Q., Zhu, X.X., 2022. Explainability analysis of cnn in detection of volcanic deformation signal, in: IGARSS 2022-2022 IEEE International Geoscience and Remote Sensing Symposium, IEEE. pp. 4851–4854.

Bi, X., Zhang, C., He, Y., Zhao, X., Sun, Y., Ma, Y., 2021. Explainable time–frequency convolutional neural network for microseismic waveform classification. *Information Sciences* 546, 883–896.

Edigbue, P., Al-Shuhail, A., Hanafy, S., 2025. Explaining deep learning models in full waveform inversion: Enhancing transparency in seismic data interpretation, in: SPE Middle East Oil and Gas Show and Conference, SPE. p. D021S047R005.

Guo, J., Tang, Z., Zhang, C., Xu, W., Wu, Y., 2023. An interpretable

deep learning method for identifying extreme events under faulty data interference. *Applied Sciences* 13, 5659.

Jena, R., Shanableh, A., Al-Ruzouq, R., Pradhan, B., Gibril, M.B.A., Khalil, M.A., Ghorbanzadeh, O., Ganapathy, G.P., Ghamisi, P., 2023. Explainable artificial intelligence (xai) model for earthquake spatial probability assessment in arabian peninsula. *Remote Sensing* 15, 2248.

Jiang, J., Stankovic, V., Stankovic, L., Murray, D., Pytharouli, S., 2024. Explainable ai for transparent seismic signal classification, in: *IGARSS 2024-2024 IEEE International Geoscience and Remote Sensing Symposium*, IEEE. pp. 8801–8805.

Li, S., Li, T., Sun, C., Yan, R., Chen, X., 2023. Multilayer grad-cam: An effective tool towards explainable deep neural networks for intelligent fault diagnosis. *Journal of manufacturing systems* 69, 20–30.

Li, Z., Kovachki, N., Azizzadenesheli, K., Liu, B., Bhattacharya, K., Stuart, A., Anandkumar, A., 2020. Fourier neural operator for parametric partial differential equations. *arXiv preprint arXiv:2010.08895* .

Lubo-Robles, D., Devegowda, D., Jayaram, V., Bedle, H., Marfurt, K.J., Pranter, M.J., 2022. Quantifying the sensitivity of seismic facies classification to seismic attribute selection: An explainable machine-learning study. *Interpretation* 10, SE41–SE69.

Lundberg, S.M., Lee, S.I., 2017. A unified approach to interpreting model predictions. *Advances in neural information processing systems* 30.

Majstorović, J., Giffard-Roisin, S., Poli, P., 2023. Interpreting convolutional neural network decision for earthquake detection with feature map visualization, backward optimization and layer-wise relevance propagation methods. *Geophysical Journal International* 232, 923–939.

Mousavi, S.M., Ellsworth, W.L., Zhu, W., Chuang, L.Y., Beroza, G.C., 2020. Earthquake transformer—an attentive deep-learning model for simultaneous earthquake detection and phase picking. *Nature communications* 11, 3952.

Myren, S., Parikh, N., Rael, R., Flynn, G., Higdon, D., Casleton, E., 2025. Evaluation of seismic artificial intelligence with uncertainty. *Seismological Research Letters* doi:10.1785/0220240444.

Noh, K., Kim, D., Byun, J., 2023. Explainable deep learning for supervised seismic facies classification using intrinsic method. *IEEE Transactions on Geoscience and Remote Sensing* 61, 1–11.

Park, Y., Delbridge, B.G., Shelly, D.R., 2024. Making phase-picking neural networks more consistent and interpretable. *The Seismic Record* 4, 72–80.

Saikia, P., Nankani, D., Baruah, R.D., 2019. Seismic signal interpretation for reservoir facies classification, in: *International Conference on Pattern Recognition and Machine Intelligence*, Springer. pp. 409–417.

Selvaraju, R.R., Cogswell, M., Das, A., Vedantam, R., Parikh, D., Batra, D., 2017. Grad-cam: Visual explanations from deep networks via gradient-based localization, in: *Proceedings of the IEEE international conference on computer vision*, pp. 618–626.

Sun, R., Qi, W., Zheng, T., Qi, J., 2023. Explainable machine-learning predictions for peak ground acceleration. *Applied Sciences* 13. URL: <https://www.mdpi.com/2076-3417/13/7/4530>, doi:10.3390/app13074530.

Trani, L., Pagani, G.A., Zanetti, J.P.P., Chapeland, C., Evers, L., 2022. Deepquake—an application of cnn for seismo-acoustic event classification in the netherlands. *Computers & Geosciences* 159, 104980.

Wang, X., Wei, Z., Wang, Z., Wei, S., Li, Y., Shahzad, M.M., 2025. Explainable ai-driven optimal feature selection for the identification of structural damage. *Structural Control and Health Monitoring* 2025, 7253150. URL: <https://onlinelibrary.wiley.com/doi/abs/10.1155/stc/7253150>, doi:<https://doi.org/10.1155/stc/7253150>, arXiv:<https://onlinelibrary.wiley.com/doi/pdf/10.1155/stc/7253150>.

Yoo, Y., Jeong, S., 2022. Vibration analysis process based on spectrogram using gradient class activation map with selection process of cnn model and feature layer. *Displays* 73, 102233.

Zhu, W., Beroza, G.C., 2019. Phasenet: a deep-neural-network-based seismic arrival-time picking method. *Geophysical Journal International* 216, 261–273.